Parameter identification and optimization in piezoelectric energy harvesting: analytical relations, asymptotic analyses, and experimental validations

A Erturk[1]* and **D J Inman**[2]

[1]George W Woodruff School of Mechanical Engineering, Georgia Institute of Technology, Atlanta, Georgia, USA

[2]Center for Intelligent Material Systems and Structures, Virginia Polytechnic Institute and State University, Blacksburg, Virginia, USA

The manuscript was received on 31 August 2010 and was accepted after revision for publication on 10 December 2010

DOI: 10.1177/0959651810396280

Abstract: Mathematical analyses of distributed-parameter piezoelectric energy harvester equations are presented for parameter identification and optimization. The focus is placed on the single-mode voltage and vibration frequency response functions (FRFs) per translational base acceleration. Asymptotic trends of the voltage output and the tip displacement FRFs are investigated and expressions are obtained for the extreme conditions of the load resistance. The relationship between the linear voltage asymptotes and the optimal load resistance is discussed. Resonance frequencies of the voltage and the tip displacement FRFs are obtained accounting for the presence of mechanical losses. Closed-form expressions are extracted for the optimal electrical loads of maximum power generation at the short-circuit and open-circuit resonance frequencies of the voltage FRF. Analytical relations are given also for the identification of modal mechanical damping both from the voltage and the vibration FRFs using a single data point. Vibration attenuation and amplification due to resonance frequency shift is also addressed. An experimental case study is presented to validate some of the major equations derived here.

Keywords: piezoelectricity, energy harvesting, parameter identification, electromechanical systems

1 INTRODUCTION

Vibration-based energy harvesting using piezoelectric transduction has become a promising research field over the past decade due to the reduced power requirements of small electronic components, such as the sensor networks used in monitoring applications [**1**, **2**]. The motivation for vibration-based energy harvesting is to power such devices by using the vibrational energy available in their environment. Researchers have investigated both linear [**3–16**] and non-linear [**17–26**] vibration-based energy harvesting focusing on various transduction mechanisms. Piezoelectric transduction offers larger power density and higher voltage outputs compared to other transductions [**1**, **2**]. Moreover, piezoelectric materials can be fabricated in micro-scale [**27**] (which is challenging in electromagnetic energy harvesting), they do not require bias voltage (unlike in electrostatic energy harvesting) and are easy to use in multifunctional applications as structural components [**28**, **29**]. Unless it is used as a surface patch, a piezo-stack or a cymbal arrangement, typically, a piezoelectric energy harvester is a cantilevered thin beam with piezoceramic layers and it is located on a vibrating host structure for electrical power generation from bending vibrations.

**Corresponding author: George W Woodruff School of Mechanical Engineering, Georgia Institute of Technology, Atlanta, GA 30332, USA.*
email: alper.erturk@me.gatech.edu

Various papers have appeared on mathematical modelling of cantilevered piezoelectric energy harvesters. The preliminary modelling efforts [**3**], lumped-parameter modelling approaches [**4**, **5**] and analyses [**6**] were followed by distributed-parameter models [**7**–**16**] targeting better accuracy in predicting the electromechanical behaviour of the physical system. The existing distributed-parameter models include analytical solutions [**7**], energy-based approximate analytical solutions using the Rayleigh–Ritz method [**8**–**11**] and the assumed-modes method [**12**] as well as finite-element solutions [**13**–**16**].

This paper employs the distributed-parameter analytical solution [**7**] in mathematical analyses of the resulting electromechanical frequency response functions (FRFs) for parameter identification and optimization. Most of the modelling papers appeared in the literature [**5**, **9**, **11**] have made certain assumptions on mechanical damping in identifying the system parameters (an exception is a lumped-parameter analysis [**6**] given recently). Here, the expressions are given for an underdamped system by accounting for the mechanical losses. Basic trends in the voltage-output-to-base acceleration and the tip-displacement-to-base acceleration FRFs are investigated and analytical relations are obtained for the extreme conditions of the load resistance. Linear asymptotic behaviours close to short-circuit and open-circuit conditions are verified and the equations of these asymptotes are presented. Closed-form expressions are given for the optimal electrical loads of maximum power generation at the short-circuit and open-circuit resonance frequencies of the voltage FRF. The relationship between the voltage asymptotes and the optimal electrical loads at these frequencies is addressed. As an alternative to conventional techniques of damping identification, expressions are given also for the identification of modal mechanical damping either from the voltage FRF or from the vibration FRF using only a single data point. Vibration attenuation and amplification resulting from the resonance frequency shift is also discussed. An experimental case study is presented for a brass-reinforced PZT-5H bimorph for validation of the expressions given here.

2 DISTRIBUTED-PARAMETER ELECTROMECHANICAL MODEL

The electromechanical model that forms the basis of this work is the experimentally validated distributed-parameter analytical solution [**7**]. Figure 1 shows symmetric bimorph piezoelectric energy harvester configurations under base excitation (in the form of

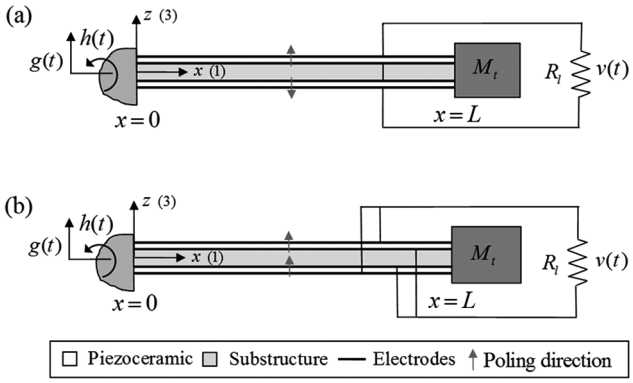

Fig. 1 Bimorph piezoelectric energy harvester configurations under base excitation: (a) series connection and (b) parallel connection

translational displacement $g(t)$ with superimposed small rotational displacement $h(t)$). The perfectly conductive electrodes of negligible thickness covering the surfaces of the piezoceramic layers are connected to a resistive electrical load (R_l). The electromechanical formulation is based on the Euler–Bernoulli beam assumptions. Therefore the structural configurations considered here are assumed to be sufficiently thin so that the shear deformation and rotary inertia effects are negligible (modelling of moderately thick piezoelectric energy harvester configurations based on the Timoshenko beam assumptions can be found in Erturk and Inman [**12**]).

If the base motion in Fig. 1 is harmonic of the form $g(t) = W_0 e^{j\omega t}$ and $h(t) = \theta_0 e^{j\omega t}$ (where W_0 and θ_0, respectively, are the translational and small rotational displacement amplitudes of the base, ω is the excitation frequency and j is the unit imaginary number), the steady-state voltage response across the load can be given in the form [**7**]

$$v(t) = \frac{\sum_{r=1}^{\infty} \frac{j\omega\chi_r F_r(\omega) e^{j\omega t}}{\omega_r^2 - \omega^2 + j2\zeta_r\omega_r\omega}}{\frac{1}{R_l} + j\omega C_p^{eq} + \sum_{r=1}^{\infty} \frac{j\omega\chi_r^2}{\omega_r^2 - \omega^2 + j2\zeta_r\omega_r\omega}} \tag{1}$$

where ω_r is the undamped natural frequency in short-circuit conditions (i.e. under constant electric field conditions of the piezoceramic layers), ζ_r is the mechanical damping ratio, $F_r(\omega)$ is the mechanical forcing function, χ_r is the electromechanical coupling term of the rth vibration mode and C_p^{eq} is the equivalent inherent capacitance of the piezoceramic layers. The modal electromechanical coupling and the equivalent inherent capacitance terms for the series and parallel connections of the piezoceramic layers are as given in Table 1, where $\bar{e}_{31}$ is the effective piezoelectric stress constant and $\bar{\varepsilon}_{33}^S$ is the permittivity component at constant strain and an over-

Table 1 Modal electromechanical coupling and equivalent capacitance terms for the (a) series, and (b) parallel connection cases

(a) Series connection	
χ_r	$-\bar{e}_{31}(h_p + h_s)b\phi_r'(L)/2$
C_p^{eq}	$\bar{\varepsilon}_{33}^{S} bL/2h_p$
(b) Parallel connection	
χ_r	$-\bar{e}_{31}(h_p + h_s)b\phi_r'(L)$
C_p^{eq}	$2\bar{\varepsilon}_{33}^{S} bL/h_p$

bar denotes that the respective parameter is given for the plane-stress conditions of a thin beam [**7**] (in terms of the three-dimensional constants, $\bar{e}_{31} = d_{31}/s_{11}^{E}$, $\bar{c}_{11}^{E} = 1/s_{11}^{E}$ and $\bar{\varepsilon}_{33}^{S} = \varepsilon_{33}^{T} - d_{31}^2/s_{11}^{E}$ where d_{31} is the piezoelectric strain constant, s_{11}^{E} is the elastic compliance at constant electric field and ε_{33}^{T} is the permittivity constant at constant stress). In Table 1, $\phi_r(x)$ is the mass normalized eigenfunction of a clamped-free beam (with a tip mass) of the rth vibration mode [**7**] ($\phi_r'(x)$ is its derivative with respect to x), b and L are the width and the length of the beam, respectively, h_p is the thickness of each piezoceramic layer and h_s is the thickness of the substructure layer.

The modal mechanical forcing function due to base excitation is

$$F_r(\omega) = \omega^2 W_0 \left(m \int_0^L \phi_r(x)\,\mathrm{d}x + M_t \phi_r(L) \right) + \omega^2 \theta_0 \left(\int_0^L x\phi_r(x)\,\mathrm{d}x + M_t L \phi_r(L) \right) \tag{2}$$

where m is the mass per length of the beam and M_t is the tip mass.

The electromechanically coupled vibration response of the energy harvester beam (relative to its moving base) at steady state is

$$w_{rel}(x,t) = \sum_{r=1}^{\infty} \frac{[F_r(\omega) - \chi_r v(t)]\phi_r(x)\mathrm{e}^{\mathrm{j}\omega t}}{{\omega_r}^2 - \omega^2 + \mathrm{j}2\zeta_r\omega_r\omega} \tag{3}$$

which includes the effect of piezoelectric shunt damping due to the $\chi_r v(t)$ term, where $v(t)$ is given by equation (1).

3 SINGLE-MODE ELECTROMECHANICAL FRFS

3.1 Complex forms

Hereafter it is assumed that the base does not rotate and focus on the electromechanical FRFs that relate the response to the translational base acceleration in the transverse direction. Furthermore, if the excitation frequency is very close to a natural frequency, that is $\omega \cong \omega_r$, the following FRFs can be extracted from equations (1) and (3)

$$\hat{\alpha}(\omega) = \frac{\hat{v}(t)}{-\omega^2 W_0 \mathrm{e}^{\mathrm{j}\omega t}} = \frac{\mathrm{j}\omega R_l \chi_r \sigma_r}{\left(1 + \mathrm{j}\omega R_l C_p^{eq}\right)\left({\omega_r}^2 - \omega^2 + \mathrm{j}2\zeta_r\omega_r\omega\right) + \mathrm{j}\omega R_l \chi_r^2} \tag{4}$$

$$\hat{\beta}(\omega, x) = \frac{\hat{w}_{rel}(x,t)}{-\omega^2 W_0 \mathrm{e}^{\mathrm{j}\omega t}} = \frac{\left(1 + \mathrm{j}\omega R_l C_p^{eq}\right)\sigma_r \phi_r(x)}{\left(1 + \mathrm{j}\omega R_l C_p^{eq}\right)\left({\omega_r}^2 - \omega^2 + \mathrm{j}2\zeta_r\omega_r\omega\right) + \mathrm{j}\omega R_l \chi_r^2} \tag{5}$$

where

$$\sigma_r = -m \int_0^L \phi_r(x)\,\mathrm{d}x - M_t \phi_r(L) \tag{6}$$

and the hat (^) denotes that the respective expression is given for a single vibration mode. Equations (4) and (5), respectively, are the single-mode voltage output to translational base acceleration and displacement response to translational base acceleration FRFs. These expressions are the *complex forms* of the single-mode electromechanical FRFs.

3.2 Magnitude-phase forms

The single-mode voltage FRF can be expressed in the magnitude-phase form as

$$\hat{\alpha}(\omega) = |\hat{\alpha}(\omega)|\mathrm{e}^{\mathrm{j}\Phi(\omega)} \tag{7}$$

where the magnitude (the modulus) of the FRF is

$$|\hat{\alpha}(\omega)| = \frac{\omega R_l |\chi_r \sigma_r|}{\left\{\left[{\omega_r}^2 - \omega^2\left(1 + 2R_l C_p^{eq}\omega_r\zeta_r\right)\right]^2 + \left[2\zeta_r\omega_r\omega + R_l\omega\left(C_p^{eq}\omega_r^2 - C_p^{eq}\omega^2 + \chi_r^2\right)\right]^2\right\}^{1/2}} \tag{8}$$

and the phase (the argument) is

$$\Phi(\omega) = \frac{\pi}{2}\mathrm{sgn}(\chi_r\sigma_r) - \tan^{-1}\left(\frac{2\zeta_r\omega_r\omega + R_l\omega\left(C_p^{eq}\omega_r^2 - C_p^{eq}\omega^2 + \chi_r^2\right)}{{\omega_r}^2 - \omega^2\left(1 + 2R_l C_p^{eq}\omega_r\zeta_r\right)}\right) \tag{9}$$

where sgn stands for the signum function.

The single-mode tip displacement FRF is then

$$\hat{\beta}(\omega, x) = \left|\hat{\beta}(\omega, x)\right|\mathrm{e}^{\mathrm{j}\Psi(\omega, x)} \tag{10}$$

where its magnitude and phase are

$$\left|\hat{\beta}(\omega,x)\right| = \frac{|\sigma_r \phi_r(x)|\left[1+\left(\omega R_{\mathrm{l}} C_{\mathrm{p}}^{\mathrm{eq}}\right)^2\right]^{1/2}}{\left\{\left[{\omega_r}^2-\omega^2\left(1+2R_{\mathrm{l}}C_{\mathrm{p}}^{\mathrm{eq}}\omega_r\zeta_r\right)\right]^2+\left[2\zeta_r\omega_r\omega+R_{\mathrm{l}}\omega\left(C_{\mathrm{p}}^{\mathrm{eq}}\omega_r^2-C_{\mathrm{p}}^{\mathrm{eq}}\omega^2+\chi_r^2\right)\right]^2\right\}^{1/2}} \tag{11}$$

$$\Psi(\omega,x) = \tan^{-1}\left(\frac{\omega R_{\mathrm{l}} C_{\mathrm{p}}^{\mathrm{eq}}\sigma_r\phi_r(x)}{\sigma_r\phi_r(x)}\right) - \tan^{-1}\left[\frac{2\zeta_r\omega_r\omega+R_{\mathrm{l}}\omega\left(C_{\mathrm{p}}^{\mathrm{eq}}\omega_r{}^2-C_{\mathrm{p}}^{\mathrm{eq}}\omega^2+\chi_r^2\right)}{\omega_r^2-\omega^2\left(1+2R_{\mathrm{l}}C_{\mathrm{p}}^{\mathrm{eq}}\omega_r\zeta_r\right)}\right] \tag{12}$$

3.3 Dimensionless forms

Some of the terms in the magnitude and phase of the voltage FRF can be put into dimensionless forms to give

$$|\hat{\alpha}(\tilde{\omega})| = \frac{\tilde{\omega}\gamma_r\upsilon_r|\sigma_r/\chi_r|}{\left\{\left[1-\tilde{\omega}^2(1+2\upsilon_r\zeta_r)\right]^2+\left[(2\zeta_r+\upsilon_r(1+\gamma_r))\tilde{\omega}-\upsilon_r\tilde{\omega}^3\right]^2\right\}^{1/2}} \tag{13}$$

$$\Phi(\tilde{\omega}) = \frac{\pi}{2}\mathrm{sgn}\left(\frac{\sigma_r}{\chi_r}\right) - \tan^{-1}\left[\frac{(2\zeta_r+\upsilon_r(1+\gamma_r))\tilde{\omega}-\upsilon_r\tilde{\omega}^3}{1-\tilde{\omega}^2(1+2\upsilon_r\zeta_r)}\right] \tag{14}$$

Similarly, the magnitude and phase of the tip displacement FRF become

$$|\hat{\beta}(\tilde{\omega},x)| = \frac{|f_r(x)|\left[1+(\tilde{\omega}\upsilon_r)^2\right]^{1/2}}{\omega_r^2\left\{\left[1-\tilde{\omega}^2(1+2\upsilon_r\zeta_r)\right]^2+\left[(2\zeta_r+\upsilon_r(1+\gamma_r))\tilde{\omega}-\upsilon_r\tilde{\omega}^3\right]^2\right\}^{1/2}} \tag{15}$$

$$\Psi(\tilde{\omega},x) = \tan^{-1}\left(\frac{\tilde{\omega}\upsilon_r f_r(x)}{f_r(x)}\right) - \tan^{-1}\left[\frac{(2\zeta_r+\upsilon_r(1+\gamma_r))\tilde{\omega}-\upsilon_r\tilde{\omega}^3}{1-\tilde{\omega}^2(1+2\upsilon_r\zeta_r)}\right] \tag{16}$$

In equations (13) to (16), the dimensionless terms are

$$\upsilon_r = R_{\mathrm{l}}C_{\mathrm{p}}^{\mathrm{eq}}\omega_r,\ \gamma_r = \frac{\chi_r^2}{C_{\mathrm{p}}^{\mathrm{eq}}\omega_r^2},\ \tilde{\omega} = \frac{\omega}{\omega_r},\ f_r(x) = \sigma_r\phi_r(x) \tag{17}$$

Note that the modulus of the voltage FRF given by equation (13) has the units of [Vs^2/m] due to σ_r/χ_r while the modulus of the tip displacement FRF given by equation (15) has the units of [s^2] due to $1/\omega_r^2$.

4 ASYMPTOTIC ANALYSES AND RESONANCE FREQUENCIES

4.1 Short-circuit and open-circuit asymptotes of the voltage FRF

Taking the limit as $\upsilon_r \to 0$ yields the following expression for very small values of load resistance. Note that $\upsilon_r \to 0$ implies $R_{\mathrm{l}} \to 0$ (short-circuit conditions) and $\upsilon_r \to \infty$ implies $R_{\mathrm{l}} \to \infty$ (open-circuit conditions) according to equation (17.1).

$$|\hat{\alpha}_{\mathrm{sc}}(\tilde{\omega})| = \lim_{\upsilon_r\to 0}|\hat{\alpha}(\tilde{\omega})| = \frac{\tilde{\omega}\gamma_r\upsilon_r|\sigma_r/\chi_r|}{\left[\left(1-\tilde{\omega}^2\right)^2+\left(2\zeta_r\tilde{\omega}\right)^2\right]^{1/2}} \tag{18}$$

The limit $\upsilon_r \to \infty$ leads to the following relation for very large values of load resistance

$$|\hat{\alpha}_{\mathrm{oc}}(\tilde{\omega})| = \lim_{\upsilon_r\to\infty}|\hat{\alpha}(\tilde{\omega})| = \frac{\gamma_r|\sigma_r/\chi_r|}{\left\{\left[(1+\gamma_r)-\tilde{\omega}^2\right]^2+\left(2\zeta_r\tilde{\omega}\right)^2\right\}^{1/2}} \tag{19}$$

Here, the subscripts sc and oc stand for the *short-circuit* and the *open-circuit* conditions. Equations (18) and (19) represent the moduli of the voltage FRF for the extreme cases of the load resistance ($R_{\mathrm{l}} \to 0$ and $R_{\mathrm{l}} \to \infty$, respectively). It is useful to note that the short-circuit voltage asymptote depends on the load resistance linearly whereas the open-circuit voltage asymptote does not depend on the load resistance. Asymptotes of the current FRF are not discussed here and they can easily be derived from the voltage asymptotes.

4.2 Short-circuit and open-circuit asymptotes of the tip displacement FRF

The asymptotic behaviours for the short-circuit and the open-circuit conditions of the tip displacement FRF are

$$\left|\hat{\beta}_{\mathrm{sc}}(\tilde{\omega},x)\right| = \lim_{\upsilon_r\to 0}\left|\hat{\beta}(\tilde{\omega},x)\right| = \frac{|f_r(x)|}{{\omega_r}^2\left[\left(1-\tilde{\omega}^2\right)^2+\left(2\zeta_r\tilde{\omega}\right)^2\right]^{1/2}} \tag{20}$$

$$|\hat{\beta}_{\text{oc}}(\tilde{\omega}, x)| = \lim_{\upsilon_r \to \infty} |\hat{\beta}(\tilde{\omega}, x)| = \frac{|f_r(x)|}{\omega_r{}^2 \left\{ \left[(1+\gamma_r) - \tilde{\omega}^2 \right]^2 + (2\zeta_r \tilde{\omega})^2 \right\}^{1/2}} \quad (21)$$

Note that the short-circuit and the open-circuit asymptotes obtained for the vibration response of the beam do *not* depend on the load resistance.

4.3 Short-circuit and open-circuit resonance frequencies of the voltage FRF

Having obtained the magnitude of the voltage FRF for electrical loads close to short-circuit conditions, one can find its dimensionless resonance frequency ($\tilde{\omega}_{\text{vsc}}^{\text{res}}$) as

$$\left. \frac{\partial |\hat{\alpha}_{\text{sc}}(\tilde{\omega})|}{\partial \tilde{\omega}} \right|_{\tilde{\omega}_{\text{vsc}}^{\text{res}}} = 0 \rightarrow \tilde{\omega}_{\text{vsc}}^{\text{res}} = 1 \quad (22)$$

Therefore the dimensionless resonance frequency ($\tilde{\omega}_{\text{vsc}}^{\text{res}}$) of the voltage FRF for very low values of load resistance is simply unity.

Similarly, the dimensionless resonance frequency ($\tilde{\omega}_{\text{voc}}^{\text{res}}$) of the voltage FRF for very large values of load resistance is obtained as

$$\left. \frac{\partial |\hat{\alpha}_{\text{oc}}(\tilde{\omega})|}{\partial \tilde{\omega}} \right|_{\tilde{\omega}_{\text{voc}}^{\text{res}}} = 0 \rightarrow \tilde{\omega}_{\text{voc}}^{\text{res}} = \left(1 + \gamma_r - 2\zeta_r^2\right)^{1/2} \quad (23)$$

4.4 Short-circuit and open-circuit resonance frequencies of the tip displacement FRF

Using the short-circuit asymptote of the tip displacement FRF, the dimensionless resonance frequency ($\tilde{\omega}_{\text{wsc}}^{\text{res}}$) of the tip displacement FRF for very low values of load resistance is obtained as

$$\left. \frac{\partial |\hat{\beta}_{\text{sc}}(\tilde{\omega}, x)|}{\partial \tilde{\omega}} \right|_{\tilde{\omega}_{\text{wsc}}^{\text{res}}} = 0 \rightarrow \tilde{\omega}_{\text{wsc}}^{\text{res}} = \left(1 - 2\zeta_r^2\right)^{1/2} \quad (24)$$

The dimensionless resonance frequency ($\tilde{\omega}_{\text{woc}}^{\text{res}}$) of the tip displacement FRF for very large values of load resistance is

$$\left. \frac{\partial |\hat{\beta}_{\text{oc}}(\tilde{\omega}, x)|}{\partial \tilde{\omega}} \right|_{\tilde{\omega}_{\text{woc}}^{\text{res}}} = 0 \rightarrow \tilde{\omega}_{\text{woc}}^{\text{res}} = \left(1 + \gamma_r - 2\zeta_r^2\right)^{1/2} \quad (25)$$

4.5 Comparison of the short-circuit and the open-circuit resonance frequencies

Note that the dimensionless short-circuit resonance frequencies of the voltage and the tip displacement FRFs are *not* the same. The short-circuit resonance frequency of the voltage FRF does *not* depend on mechanical damping whereas the open-circuit resonance frequencies of both FRFs depend on mechanical damping. The mechanically undamped short-circuit and open-circuit natural frequencies of the voltage and tip displacement FRFs, however, are identical, that is $\tilde{\omega}_r^{\text{sc}} = 1$ and $\tilde{\omega}_r^{\text{oc}} = (1+\gamma_r)^{1/2}$ for $\zeta_r = 0$ (which is the conventional [**30**] mechanically lossless scenario). These undamped forms are obtained through optimizing the power output in duToit *et al.* [**5**, **9**] and Kim *et al.* [**11**] by ignoring the mechanical damping. Later, Renno *et al.* [**6**] improved their [**5**, **9**, **11**] expressions by considering the presence of mechanical damping and provided a rigorous analysis for bifurcations of the frequencies of the maximum power output with changing mechanical damping.

In the present work, the short-circuit and the open-circuit resonance frequencies are defined based on the voltage FRF. One can express the single-mode approximations of these dimensionless frequencies (note that these are not necessarily the frequencies of the maximum power output [**6**]. They are the resonance frequencies of the voltage FRF for very small and very large values of load resistance) as

$$\tilde{\omega}_r^{\text{sc}} = 1 \quad (26)$$

$$\tilde{\omega}_r^{\text{oc}} = \left(1 + \gamma_r - 2\zeta_r^2\right)^{1/2} \quad (27)$$

The dimensional forms are then

$$\omega_r^{\text{sc}} = \omega_r \quad (28)$$

$$\omega_r^{\text{oc}} = \omega_r \left(1 + \gamma_r - 2\zeta_r^2\right)^{1/2} \quad (29)$$

Therefore the resonance frequency shift in the voltage-to-base acceleration FRF as the load resistance is increased from $R_{\text{l}} \rightarrow 0$ to $R_{\text{l}} \rightarrow \infty$ is

$$\Delta\omega = \omega_r^{\text{oc}} - \omega_r^{\text{sc}} = \omega_r \left[\left(1 + \gamma_r - 2\zeta_r^2\right)^{1/2} - 1 \right] \quad (30)$$

According to equation (30), the resonance frequency shift from the short-circuit to the open-circuit conditions is proportional to γ_r. It follows from equation (17.2) that $\Delta\omega$ is directly proportional to the square of the modal electromechanical coupling term (χ_r^2), inversely proportional to the equivalent capacitance (C_{p}^{eq}) and square of the undamped natural frequency in short-circuit

conditions (ω_r^2). The resonance frequency shift is affected by the modal mechanical damping ratio (ζ_r) as well. According to equation (30), mechanical losses counteract the effect of electromechanical coupling. Theoretically, the open-circuit resonance frequency can be equal to the short-circuit resonance frequency for $2\zeta_r^2 = \gamma_r$. Physically, this condition implies large mechanical losses and/or relatively small electromechanical coupling. The focus in this paper is, however, placed on strongly coupled and lightly damped energy harvesters (as in the experimental case study of section 8).

5 IDENTIFICATION OF MECHANICAL DAMPING

In the electromechanical system, one can identify the mechanical damping ratio either using the voltage FRF or using the vibration FRF. The following derivations provide closed-form expressions for the identification of mechanical damping at $\tilde{\omega} = \tilde{\omega}_{\text{sc}}$ in the presence of an arbitrary load resistance using both approaches (which can also be given for $\tilde{\omega} = \tilde{\omega}_r^{\text{oc}}$ following a similar way). Although it is usual to identify mechanical damping from vibration measurements, voltage measurements can be preferred for cantilevers in micro-scale in the absence of vibration measurement equipment.

5.1 Identification of the modal mechanical damping ratio from the voltage FRF

In order to identify the modal mechanical damping ratio for an arbitrary but non-zero value of the dimensionless resistance υ_r, one can set $\tilde{\omega} = 1$ in equation (13) to obtain

$$|\hat{\alpha}(1)| = \frac{\gamma_r \upsilon_r |\sigma_r / \chi_r|}{\left[(2\upsilon_r \zeta_r)^2 + (2\zeta_r + \upsilon_r \gamma_r)^2 \right]^{1/2}} \tag{31}$$

where $|\hat{\alpha}(1)|$ is known from the experimental measurement (i.e. it is the experimental data point used for damping identification). Equation (31) yields the quadratic relation

$$A\zeta_r^2 + B\zeta_r + C = 0 \tag{32}$$

where

$$A = 4\left(1 + \upsilon_r^2\right), B = 4\gamma_r \upsilon_r, C = \upsilon_r^2 \gamma_r^2 - \left(\frac{\gamma_r \upsilon_r \sigma_r}{|\hat{\alpha}(1)| \chi_r} \right)^2 \tag{33}$$

The positive root of equation (32) gives the modal mechanical damping ratio as

$$\zeta_r = \frac{\left(B^2 - 4AC\right)^{1/2} - B}{2A} \tag{34}$$

Although υ_r (the dimensionless measure of load resistance) is arbitrary in identifying the mechanical damping ratio from the mathematical point of view, physically, it should be large enough so that $|\hat{\alpha}(1)|$ is a meaningful voltage FRF measurement (i.e. not noise) with acceptable coherence.

5.2 Identification of the modal mechanical damping ratio from the tip displacement FRF

Identification of the modal mechanical damping from the vibration measurement requires using equation (15). If the frequency of interest is again $\tilde{\omega} = 1$, equation (15) becomes

$$\left|\hat{\beta}(1, x)\right| = \frac{|f_r(x)| \left(1 + \upsilon_r^2\right)^{1/2}}{\omega_r^2 \left[(2\upsilon_r \zeta_r)^2 + (2\zeta_r + \upsilon_r \gamma_r)^2 \right]^{1/2}} \tag{35}$$

which yields an alternative quadratic equation of the form given by equation (32), where the coefficients are

$$A = 4\left(1 + \upsilon_r^2\right), B = 4\gamma_r \upsilon_r, \quad C = \upsilon_r^2 \gamma_r^2 - \frac{|f_r(x)|^2 \left(1 + \upsilon_r^2\right)}{\omega_r^4 \left|\hat{\beta}(1, x)\right|^2} \tag{36}$$

The modal mechanical damping ratio is then the positive root of equation (32) for the coefficients given by equation (36). When using these closed-form equations for damping identification, one should first make sure to check that the model prediction of the respective experimental short-circuit resonance frequency is sufficiently accurate. Note that the value of $\left|\hat{\beta}(1, x)\right|$ at point x on the beam is the experimental data point used in the identification process (for $\tilde{\omega} = 1$). Unlike the case of mechanical damping identification using the voltage FRF, the external load resistance can be chosen very close to zero here (since such a load does not cause noise in the vibration FRF). In fact, for $\upsilon_r \to 0$ (shorting the electrodes), equation (35) simplifies to the purely mechanical form of

$$\zeta_r = \frac{|f_r(x)|}{2\omega_r^2 \left|\hat{\beta}(1, x)\right|} \tag{37}$$

6 IDENTIFICATION OF THE OPTIMAL ELECTRICAL LOAD FOR RESONANCE EXCITATION

6.1 Electrical power FRF

Using the voltage FRF given by equation (13), the electrical power FRF is obtained as

$$\left|\hat{\Pi}(\tilde{\omega})\right| = \frac{(\tilde{\omega}\gamma_r \upsilon_r \sigma_r/\chi_r)^2/R_l}{\left[1-\tilde{\omega}^2(1+2\upsilon_r\zeta_r)\right]^2+\left[(2\zeta_r+\upsilon_r(1+\gamma_r))\tilde{\omega}-\upsilon_r\tilde{\omega}^3\right]^2} \tag{38}$$

For excitation at the short-circuit resonance frequency, $\tilde{\omega}=1$, the electrical power FRF is

$$\left|\hat{\Pi}(1)\right| = \frac{(\gamma_r\sigma_r/\chi_r)^2/R_l}{(2\zeta_r)^2+(2\zeta_r/\upsilon_r+\gamma_r)^2} \tag{39}$$

and for excitation at the open-circuit resonance frequency, $\tilde{\omega}=\left(1+\gamma_r-2\zeta_r^2\right)^{1/2}$, the electrical power FRF becomes

$$\left|\hat{\Pi}\left(\left(1+\gamma_r-2\zeta_r^2\right)^{1/2}\right)\right| = \frac{(\gamma_r\upsilon_r\sigma_r/\chi_r)^2/R_l}{\left[1-\left(1+\gamma_r-2\zeta_r^2\right)(1+2\upsilon_r\zeta_r)\right]^2/\left(1+\gamma_r-2\zeta_r^2\right)+\left[2\zeta_r(1+\zeta_r\upsilon_r)\right]^2} \tag{40}$$

6.2 Optimal values of load resistance at the short-circuit and open-circuit resonance frequencies of the voltage FRF

Equation (38) can be used in order to obtain the optimal load resistance for the maximum electrical power output at a given excitation frequency $\tilde{\omega}$ (around the respective resonance frequency). If the problem of interest is resonance excitation, one can use equation (39) to obtain

$$\left.\frac{\partial\left|\hat{\Pi}(1)\right|}{\partial R_l}\right|_{R_l^{\text{opt},\tilde{\omega}=1}} = 0 \rightarrow R_l^{\text{opt},\tilde{\omega}=1} = \frac{1}{\omega_r C_p^{eq}\left[1+(\gamma_r/2\zeta_r)^2\right]^{1/2}} \tag{41}$$

which is the optimal load resistance for excitation at the short-circuit resonance frequency of the voltage FRF. A similar way can be followed for estimating the optimal load resistance for excitation at the open-circuit resonance frequency of the voltage FRF as

$$\left.\frac{\partial\left|\hat{\Pi}\left(\left(1+\gamma_r-2\zeta_r^2\right)^{1/2}\right)\right|}{\partial R_l}\right|_{R_l^{\text{opt},\tilde{\omega}=\left(1+\gamma_r-2\zeta_r^2\right)^{1/2}}} = 0 \rightarrow R_l^{\text{opt},\tilde{\omega}=\left(1+\gamma_r-2\zeta_r^2\right)^{1/2}} = \frac{1}{\omega_r C_p^{eq}}\left[\frac{1-\zeta_r^2+(\gamma_r/2\zeta_r)^2}{\left(1+\gamma_r-\zeta_r^2\right)\left(1+\gamma_r-2\zeta_r^2\right)}\right]^{1/2} \tag{42}$$

For excitations at the short-circuit and open-circuit resonance frequencies of the voltage FRF the optimal values of load resistance are inversely proportional to the capacitance and the undamped natural frequency. The electromechanical coupling and the mechanical damping ratio also affect the optimal load resistance. The optimal resistive loads obtained in equations (41) and (42) can be back substituted into equations (39) and (40) to obtain the maximum power expressions for excitations at these two frequencies.

Recall that the short-circuit and the open-circuit resonance frequencies defined here (based on the voltage FRF) are not necessarily the frequencies of maximum power generation. One can first obtain $R_l^{\text{opt}}(\omega)$ from equation (38) by setting $\partial\left|\hat{\Pi}(\tilde{\omega})\right|/\partial R_l = 0$ and then reuse it in equation (38) to solve $\partial\left|\hat{\Pi}(\tilde{\omega})\right|/\partial\tilde{\omega}=0$ for the frequencies of the maximum power output (see Renno *et al.* [**6**] for a detailed analysis of this problem based on lumped-parameter modelling for a piezo-stack, which can easily be implemented to the expressions given here).

6.3 Relationship between the voltage asymptotes and the optimal load resistance

Remarkably, it can be shown that the intersection of the short-circuit and the open-circuit voltage asymptotes given by equations (18) and (19) take place at the optimal load resistance for excitations at these two frequencies:

$$|\hat{\alpha}_{sc}(1)| = |\hat{\alpha}_{oc}(1)| \rightarrow \upsilon_r = \frac{2\zeta_r}{\left[\gamma_r^2+(2\zeta_r)^2\right]^{1/2}} \tag{43}$$

$$\left|\hat{\alpha}_{sc}\left(\left(1+\gamma_r-2\zeta_r^2\right)^{1/2}\right)\right| = \left|\hat{\alpha}_{oc}\left(\left(1+\gamma_r-2\zeta_r^2\right)^{1/2}\right)\right| \rightarrow \upsilon_r = \left[\frac{1-\zeta_r^2+(\gamma_r/2\zeta_r)^2}{\left(1+\gamma_r-\zeta_r^2\right)\left(1+\gamma_r-2\zeta_r^2\right)}\right]^{1/2} \tag{44}$$

Table 2 Geometric and material properties of the PZT-5H bimorph cantilever

	Piezoceramic (PZT-5H)	Substructure (brass)
Length (L) [mm]	24.53	24.53
Width (b) [mm]	6.4	6.4
Thickness (h_p, h_s) [mm]	0.265 (each)	0.140
Mass density (ρ_p,ρ_s) [kg/m^3]	7500	9000
Elastic modulus ($\bar{c}_{11}^E$, Y_s) [GPa]	60.6	105
Piezoelectric constant ($\bar{e}_{31}$) [C/m^2]	-16.6	-
Permittivity constant ($\bar{\varepsilon}_{33}^S$) [nF/m]	25.55	-

which are equivalent to the optimal resistance values given by equations (41) and (42), respectively, for excitations at the short-circuit and the open-circuit resonance frequencies of the voltage FRF.

7 VIBRATION ATTENUATION/AMPLIFICATION FROM THE SHORT-CIRCUIT TO OPEN-CIRCUIT CONDITIONS

The ratio of the displacement response amplitude under open-circuit conditions to that under short-circuit conditions at frequency $\tilde{\omega}$ is

$$\frac{|\hat{\beta}_{oc}(\tilde{\omega},x)|}{|\hat{\beta}_{sc}(\tilde{\omega},x)|}=\frac{\left[\left(1-\tilde{\omega}^2\right)^2+\left(2\zeta_r\tilde{\omega}\right)^2\right]^{1/2}}{\left\{\left[(1+\gamma_r)-\tilde{\omega}^2\right]^2+\left(2\zeta_r\tilde{\omega}\right)^2\right\}^{1/2}} \tag{45}$$

For excitation at the short-circuit resonance frequency of the voltage FRF, $\tilde{\omega}=1$

$$\frac{|\hat{\beta}_{oc}(1,x)|}{|\hat{\beta}_{sc}(1,x)|}=\frac{1}{\left[1+\left(\gamma_r/2\zeta_r\right)^2\right]^{1/2}} \tag{46}$$

yielding a percentage vibration attenuation of

$$\delta_w(1)=\left[\frac{1}{\left(1+{\gamma_r}^2/4{\zeta_r}^2\right)^{1/2}}-1\right]\times 100 \tag{47}$$

Similarly, for excitation at the open-circuit resonance frequency of the voltage FRF, $\tilde{\omega}=\left(1+\gamma_r-2\zeta_r^2\right)^{1/2}$

$$\frac{\left|\hat{\beta}_{oc}\left(\left(1+\gamma_r-2\zeta_r^2\right)^{1/2},x\right)\right|}{\left|\hat{\beta}_{sc}\left(\left(1+\gamma_r-2\zeta_r^2\right)^{1/2},x\right)\right|}=\left[\frac{1-\zeta_r^2+\left(\gamma_r/2\zeta_r\right)^2}{1-\zeta_r^2+\gamma_r}\right]^{1/2} \tag{48}$$

Hence the percentage vibration amplification (assuming $\gamma_r>4\zeta_r^2$) at the open-circuit resonance frequency of the voltage FRF is

$$\delta_w\left(\left(1+\gamma_r-2\zeta_r^2\right)^{1/2}\right)=\left\{\left[\frac{1-\zeta_r^2+\left(\gamma_r/2\zeta_r\right)^2}{1-\zeta_r^2+\gamma_r}\right]^{1/2}-1\right\}\times 100 \tag{49}$$

Note that the foregoing expressions are obtained using the relations given for the extreme conditions of the external load ($\upsilon_r\to 0$ and $\upsilon_r\to\infty$). As a useful practice, one can express the displacement field of the energy harvester when it generates the maximum electrical power (at the optimal load of the frequency of interest). The resulting displacement field can then be used to estimate the maximum dynamic stress in the piezoceramic layers due to bending vibrations since strength is an issue for the brittle piezoceramic layers [**31**], particularly in load-bearing applications [**28**, **29**].

8 EXPERIMENTAL VALIDATIONS

This section investigates a brass-reinforced PZT-5H bimorph cantilever (T226-H4-203X, Piezo Systems Inc.) for validation of the major single-mode relations derived in this paper. The bimorph cantilever has the properties listed in Table 2 and it is clamped onto a small electromagnetic shaker for base excitation as shown in Fig. 2. The base acceleration is measured by means of a small accelerometer located on the clamp and the tip velocity response is measured by using a laser vibrometer. Low-voltage chirp signal is applied to the shaker in the FRF measurements (yielding an acceleration input less than 0.1 g) to ensure that piezoelectric non-linearities [**26**] are not pronounced. In the following, the focus is placed on the fundamental vibration mode, hence $r=1$ in the single-mode equations.

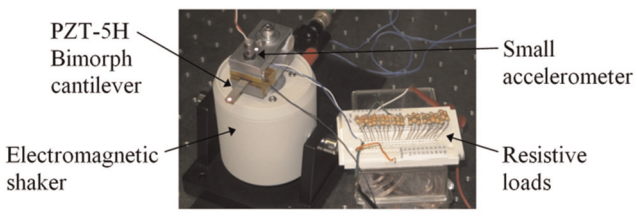

Fig. 2 PZT-5H bimorph cantilever under base excitation

8.1 Identification of mechanical damping

As an alternative to identifying the mechanical damping ratio graphically by matching the peaks in the vibration FRF (or by using conventional techniques such as the half-power points and the Nyquist plot [**32**] in frequency domain or the logarithmic decrement [**33**] in time domain), the voltage FRF is used along with the closed-form expression given by equation (34). It is first ensured that the model predicts the fundamental short-circuit resonance frequency with good accuracy for the parameters given in Table 2 (model prediction: 502.6 Hz, experimental measurement: 502.5 Hz). For a resistive load of 470 Ω, the experimental voltage amplitude at the short-circuit resonance frequency is $0.148\,\mathrm{V}/g$ (where g is the gravitational acceleration: $g = 9.81\,\mathrm{m/s^2}$). Therefore the experimental data point is $|\hat{\alpha}(1)| = 0.0151\,\mathrm{Vs^2/m}$. For this resistive load and the remaining system parameters, the coefficients in equation (32) are $A = 4.0005$, $B = 0.004\,226$, and $C = -0.000\,3469$, yielding $\zeta_1 = 0.0088$. The modal mechanical damping ratio identified from this single data point of the voltage FRF can successfully predict not only the voltage FRF (Fig. 3(a)) but also the tip velocity FRF (Fig. 3(b)). Figures 3(a) and (b), respectively, are plotted using equation (8) and a slightly modified version of equation (11) that gives the absolute tip velocity with respect to the fixed reference frame (instead of the tip displacement relative to the moving base).

8.2 Fundamental short-circuit and open-circuit resonance frequencies

The fundamental short-circuit resonance frequency (of the voltage FRF) is simply the undamped natural frequency of the cantilever as obtained in equation (28). The model [**7**] predicts this frequency as $f_1^{\mathrm{sc}} = 502.6\,\mathrm{Hz}$ (where $f_r^{\mathrm{sc}} = \omega_r^{\mathrm{sc}}/2\pi$) while the experimental value is 502.5 Hz. From equation (29), the fundamental open-circuit resonance frequency depends on γ_1 in addition to ζ_1. For the given system parameters, one obtains $\gamma_1 = 0.0940$ from equation (17.2). The fundamental open-circuit resonance frequency is then $f_1^{\mathrm{oc}} = 525.7\,\mathrm{Hz}$ (from $\tilde{\omega}_1^{\mathrm{oc}} = 1.0459$), which overestimates the experimental value of 524.7 Hz. The relative differences between these short-circuit and open-circuit resonance frequency estimates and the experimental values are +0.02 per cent and +0.2 per cent, respectively.

8.3 Magnitude and phase diagrams of the voltage FRF

The magnitude and phase diagrams of the voltage FRFs for three different resistive loads (1.2 kΩ, 44.9 kΩ and 995 kΩ) are obtained and compared against the experimental results. Figures 4(a) and (b), respectively, are plotted using equations (8) and (9) with the mechanical damping ratio (of 0.88 per cent) identified in section 8.1. The modulus expression given by equation (8) predicts the experimental

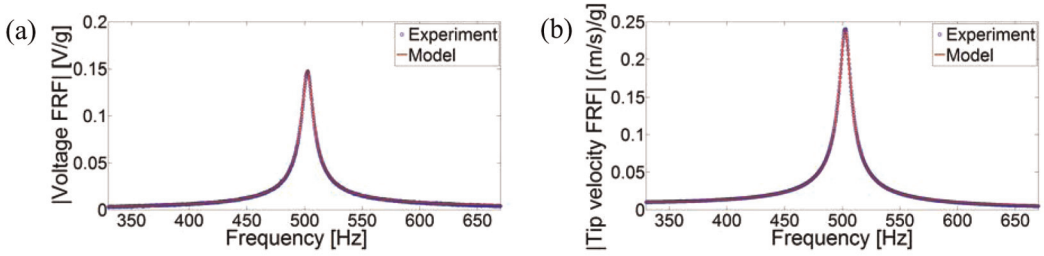

Fig. 3 (a) Voltage-to-base acceleration, and (b) tip velocity-to-base acceleration FRFs of the cantilever for $\zeta_1 = 0.0088$ ($R_l = 470\,\Omega$)

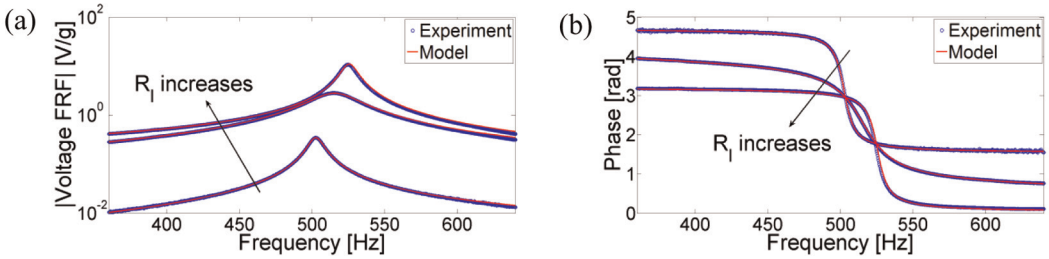

Fig. 4 (a) Magnitude, and (b) phase diagrams of the voltage FRF for three different resistive loads: 1.2 kΩ, 44.9 kΩ and 995 kΩ.

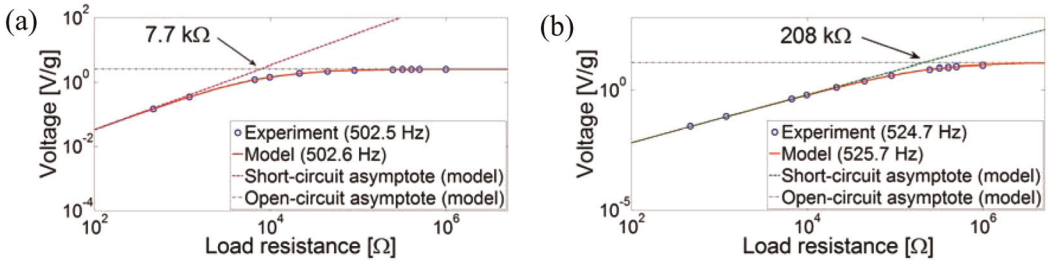

Fig. 5 Voltage versus load resistance diagrams with the linear asymptotes for excitations at the fundamental (a) short-circuit, and (b) open-circuit resonance frequencies

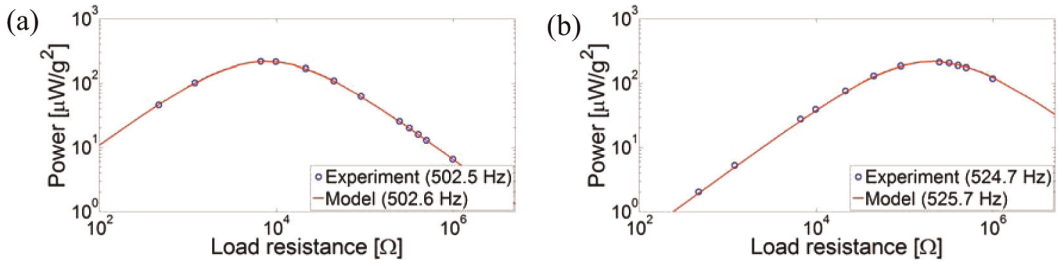

Fig. 6 Power versus load resistance diagrams for excitations at the fundamental (a) short-circuit, and (b) open-circuit resonance frequencies

voltage amplitude successfully in Fig. 4(a), and the slight inaccuracy is for the largest resistive load (due to 0.2 per cent overestimation of the open-circuit resonance frequency). The phase diagrams of these curves are also predicted very well for all three resistive loads in Fig. 4(b). It should be noted that the phase curves intersect each other at the fundamental short-circuit and open-circuit resonance frequencies.

8.4 Voltage asymptotes for resonance excitation

Variations of the voltage output obtained for $\tilde{\omega} = 1$ (dimensionless short-circuit resonance frequency) and $\tilde{\omega} = 1.0459$ (dimensionless open-circuit resonance frequency) in equation (13) are plotted in Figs 5(a) and (b), respectively, along with the linear asymptotes obtained from equations (18) and (19) at these frequencies. The analytical predictions agree very well with the experimental data while the short-circuit and the open-circuit asymptotes successfully represent the limiting trends as $R_l \to 0$ and $R_l \to \infty$. The linear asymptotes intersect at 7.7 kΩ for excitation at the short-circuit resonance frequency and at 208 kΩ for excitation at the open-circuit resonance frequency. These are expected to be the single-mode estimates of the optimal resistance for excitations at these two frequencies according to the discussion of section 6.3.

8.5 Power versus load resistance diagrams

Variation of the power output with load resistance for excitation at the fundamental short-circuit resonance frequency (of the voltage FRF) is obtained by using $\tilde{\omega} = 1$ in equation (38). Similarly, substituting $\tilde{\omega} = 1.0459$ into the same equation gives the power prediction at the fundamental open-circuit resonance frequency (of the voltage FRF). These predictions are plotted in Figs 6(a) and (b), respectively, and both of them exhibit good agreement with the experimental data. The optimal values of load resistance for excitations at the short-circuit and the open-circuit resonance frequencies are calculated by using equations (41) and (42) as 7.7 kΩ and 208 kΩ, respectively, which are indeed the intersection points of the linear voltage asymptotes shown in Fig. 5.

9 SUMMARY AND CONCLUSIONS

In this paper, mathematical analyses of the distributed-parameter electromechanical equations are presented for parameter identification and optimization. After investigating the asymptotic trends of the single-mode voltage and tip displacement FRFs for the extreme conditions of the load resistance, closed-form expressions are obtained for their short-circuit and open-circuit resonance frequencies accounting for the presence of mechanical

losses. It is shown that the short-circuit resonance frequencies of the voltage FRF and the tip displacement FRF are slightly different. Expressions for the linear asymptotes of the voltage and the tip displacement response are presented. Optimal electrical load expressions for the maximum power output at the short-circuit and the open-circuit resonance frequencies of the voltage FRF are extracted. It is observed that the intersections of the linear voltage asymptotes correspond to the respective optimal load resistance for excitations at these two frequencies. As an alternative to conventional techniques of damping identification, closed-form expressions are given for the identification of modal mechanical damping either using the voltage FRF or using the tip displacement FRF. A single data point of the voltage FRF is successfully used for identification of the modal mechanical damping ratio. This approach can be preferred for identifying mechanical damping especially for micro-scale cantilevers in the absence of vibration testing equipment. Analytical relations are given also to estimate the variation of the vibration response as the load resistance is changed between its two extrema. The experimental results of a brass-reinforced PZT-5H cantilever exhibit perfect agreement with the analytical derivations presented here.

ACKNOWLEDGEMENTS

The authors gratefully acknowledge the support from the US Air Force Office of Scientific Research under the grants F9550-06-1-0326 *Energy Harvesting and Storage Systems for Future Air Force Vehicles* and F9550-09-1-0625 *Simultaneous Vibration Suppression and Energy Harvesting* monitored by Dr B. L. Lee.

REFERENCES

1 **Anton, S. R.** and **Sodano, H. A.** A review of power harvesting using piezoelectric materials (2003–2006). *Smart Mater. Struct.*, 2007, **16**, R1–R21.
2 **Cook-Chennault, K. A., Thambi, N.,** and **Sastry, A. M.** Powering MEMS portable devices – a review of non-regenerative and regenerative power supply systems with emphasis on piezoelectric energy harvesting systems. *Smart Mater. Struct.*, 2008, **17**, 043001.
3 **Erturk, A.** and **Inman, D. J.** Issues in mathematical modeling of piezoelectric energy harvesters. *Smart Mater. Struct.*, 2008, **17**, 065016.
4 **Roundy, S.** and **Wright, P. K.** A piezoelectric vibration based generator for wireless electronics. *Smart Mater. Struct.*, 2004, **13**, 1131–1144.
5 **duToit, N. E., Wardle, B. L.,** and **Kim, S.** Design considerations for MEMS-scale piezoelectric mechanical vibration energy harvesters. *J. Integr. Ferroelectr.*, 2005, **71**, 121–160.
6 **Renno, J. M., Daqaq, F. M.,** and **Inman, D. J.** On the optimal energy harvesting from a vibration source. *J. Sound Vibr.*, 2009, **320**, 386–405.
7 **Erturk, A.** and **Inman, D. J.** An experimentally validated bimorph cantilever model for piezoelectric energy harvesting from base excitations. *Smart Mater. Struct.*, 2009, **18**, 025009.
8 **Sodano, H. A., Park, G.,** and **Inman, D. J.** Estimation of electric charge output for piezoelectric energy harvesting. *Strain*, 2004, **40**, 49–58.
9 **duToit, N. E.** and **Wardle, B. L.** Experimental verification of models for microfabricated piezoelectric vibration energy harvesters. *AIAA Journal*, 2007, **45**, 1126–1137.
10 **Elvin, N. G.** and **Elvin, A. A.** A general equivalent circuit model for piezoelectric generators. *J. Intell. Mater. Syst. Struct.*, 2009, **20**, 3–9.
11 **Kim, M., Hoegen, M., Dugundji, J.,** and **Wardle, B. L.** Modeling and experimental verification of proof mass effects on vibration energy harvester performance. *Smart Mater. Struct.*, 2010, **19**, 045023.
12 **Erturk, A.** and **Inman, D. J.** Assumed-modes formulation of piezoelectric energy harvesters: Euler–Bernoulli, Rayleigh and Timoshenko models with axial deformations. In Proceedings of the ASME 2010 ESDA 10th Biennial Conference on Engineering Systems, Design and Analysis, Istanbul, Turkey, 12–14 July 2010.
13 **Rupp, C. J., Evgrafov, A., Maute, K.,** and **Dunn, M. L.** Design of piezoelectric energy harvesting systems: a topology optimization approach based on multilayer plates and shells. *J. Intell. Mater. Syst. Struct.*, 2009, **20**, 1923–1939.
14 **De Marqui Jr., C., Erturk, A.,** and **Inman, D. J.** An electromechanical finite element model for piezoelectric energy harvester plates. *J. Sound Vibr.*, 2009, **327**, 9–25.
15 **Elvin, N. G.** and **Elvin, A. A.** A coupled finite element circuit simulation model for analyzing piezoelectric energy generators. *J. Intell. Mater. Syst. Struct.*, 2009, **20**, 587–595.
16 **Yang, Y.** and **Tang, L.** Equivalent circuit modeling of piezoelectric energy harvesters. *J. Intell. Mater. Syst. Struct.*, 2009, **20**, 2223–2235.
17 **Mann, B. P.** and **Sims, N. D.** Energy harvesting from the nonlinear oscillations of magnetic levitation. *J. Sound Vibr.*, 2009, **319**, 515–530.
18 **Ramlan, R., Brennan, M. J., Mace, B. R.,** and **Kovacic, I.** Potential benefits of a non-linear stiffness in an energy harvesting device. *Nonlin. Dynam.*, 2009, **59**, 545–558.
19 **Cottone, F., Vocca, H.,** and **Gammaitoni, L.** Nonlinear energy harvesting. *Phys. Rev. Lett.*, 2009, **102**, 080601.
20 **Gammaitoni, L., Neri, I.,** and **Vocca, H.** Nonlinear oscillators for vibration energy harvesting. *Appl. Phys. Lett.*, 2009, **94**, 164102.

21 **Erturk, A., Hoffmann, J.,** and **Inman, D. J.** A piezomagnetoelastic structure for broadband vibration energy harvesting. *Appl. Phys. Lett.*, 2009, **94**, 254102.

22 **Arrieta, A. F., Hagedorn, P., Erturk, A.,** and **Inman, D. J.** A piezoelectric bistable plate for nonlinear broadband energy harvesting. *Appl. Phys. Lett.*, 2010, **97**, 104102.

23 **Daqaq, M. F.** Response of uni-modal Duffing-type harvesters to random forced excitations. *J. Sound Vibr.*, 2010, **329**, 3621–3631.

24 **Stanton, S. C., McGehee, C. C.,** and **Mann, B. P.** Nonlinear dynamics for broadband energy harvesting: investigation of a bistable inertial generator. *Physica D*, 2010, **239**, 640–653.

25 **Barton, D. A. W., Burrow, S. G.,** and **Clare, L. R.** Energy harvesting from vibrations with a nonlinear oscillator. *ASME J. Vibr. Acoust.*, 2010, **132**, 021009.

26 **Stanton, S. C., Erturk, A., Mann, B. P.,** and **Inman, D. J.** Nonlinear piezoelectricity in electroelastic energy harvesters: modeling and experimental identification. *J. Appl. Phys.*, 2010, **108**, 074903.

27 **Choi, W. J., Jeon, Y., Jeong, J. H., Sood, R.,** and **Kim, S. G.** Energy harvesting MEMS device based on thin film piezoelectric cantilevers. *J. Electroceram.*, 2006, **17**, pp. 543–548.

28 **Anton, S. R., Erturk, A.,** and **Inman, D. J.** Multifunctional self-charging structures using piezoceramics and thin-film batteries. *Smart Mater. Struct.*, 2010, **19**, 115021.

29 **Gambier, P., Anton, S. R., Kong, N., Erturk, A.,** and **Inman, D. J.** Combined piezoelectric, solar and thermal energy harvesting for multifunctional structures with thin-film batteries. In Proceedings of the 21st International Conference on Adaptive Structures and Technologies, State College, Pennsylvania, 4–6 October 2010.

30 **Standards Committee of the IEEE Ultrasonics, Ferroelectrics, and Frequency Control Society** *IEEE Standard on Piezoelectricity*, 1987, IEEE, New York.

31 **Anton, S. R., Erturk, A.,** and **Inman, D. J.** Strength analysis of piezoceramic materials for structural considerations in energy harvesting for UAVs. *Proc. SPIE*, 2010, **7643**, 76430E.

32 **Ewins, D. J.** *Modal testing: theory, practice and application*, 2000 (Research Studies Press, Baldock, UK).

33 **Clough, R. W.** and **Penzien, J.** *Dynamics of structures*, 1975 (John Wiley and Sons, New York).